

Meteoroid mass estimation based on single-frequency radar cross section measurements

Liane Kathryn Tarnecki¹, Robert Andrew Marshall¹, Gunter Stober², and Johan Kero³

¹University of Colorado Boulder

²University of Bern

³Swedish Institute of Space Physics

November 24, 2022

Abstract

Both high-power large aperture (HPLA) radars and smaller meteor radars readily observe the dense head plasma produced as a meteoroid ablates. However, determining the mass of such meteors based on the information returned by the radar is challenging. We present a new method for deriving meteor masses from single-frequency radar measurements, using a physics-based plasma model and finite-difference time-domain (FDTD) simulations. The head plasma model derived in ¹\cite{dimopp17} depends on the meteoroids altitude, speed, and size. We use FDTD simulations of a radar pulse interacting with such head plasmas to determine the radar cross section (RCS) that a radar system would observe for a meteor with a given set of physical properties. By performing simulations over the observed parameter space, we construct tables relating meteor size, velocity, and altitude to RCS. We then use these tables to map a set of observations from the MAARSY radar (53.5 MHz) to fully-defined plasma distributions, from which masses are calculated. To validate these results, we repeat the analysis using observations of the same meteors by the EISCAT radar (929 MHz). The resulting masses are strongly linearly correlated; however, the masses derived from EISCAT measurements are on average 1.33 times larger than those derived from MAARSY measurements. Since this method does not require dual-frequency measurements for mass determination, only validation, it can be applied in the future to observations made by many single-frequency radar systems.

**Meteoroid mass estimation based on single-frequency
radar cross section measurements**

L. K. Tarnecki¹, R. A. Marshall¹, G. Stober², and J. Kero³

⁴ Smead Aerospace Engineering Sciences, University of Colorado Boulder, Boulder, Colorado, USA

⁵ Institute of Applied Physics & Oeschger Center for Climate Change Research, Microwave Physics,
⁶ University of Bern, Bern, Switzerland

⁷ Swedish Institute of Space Physics (IRF), Kiruna, Sweden

Key Points:

- ⁹ • A finite difference time domain (FDTD) model is used to simulate radar obser-
¹⁰ vations of meteors
- ¹¹ • Meteor mass estimations are made by combining observed radar cross sections with
¹² FDTD simulation results
- ¹³ • A dataset of coincident observations by two radar systems is used to verify the mass
¹⁴ estimation procedure

15 **Abstract**

16 Both high-power large aperture (HPLA) radars and smaller meteor radars readily ob-
 17 serve the dense head plasma produced as a meteoroid ablates. However, determining the
 18 mass of such meteors based on the information returned by the radar is challenging. We
 19 present a new method for deriving meteor masses from single-frequency radar measure-
 20 ments, using a physics-based plasma model and finite-difference time-domain (FDTD)
 21 simulations. The head plasma model derived in Dimant and Oppenheim (2017) depends
 22 on the meteoroids altitude, speed, and size. We use FDTD simulations of a radar pulse
 23 interacting with such head plasmas to determine the radar cross section (RCS) that a
 24 radar system would observe for a meteor with a given set of physical properties. By per-
 25 forming simulations over the observed parameter space, we construct tables relating me-
 26 teor size, velocity, and altitude to RCS. We then use these tables to map a set of obser-
 27 vations from the MAARSY radar (53.5 MHz) to fully-defined plasma distributions, from
 28 which masses are calculated. To validate these results, we repeat the analysis using ob-
 29 servations of the same meteors by the EISCAT radar (929 MHz). The resulting masses
 30 are strongly linearly correlated; however, the masses derived from EISCAT measurements
 31 are on average 1.33 times larger than those derived from MAARSY measurements. Since
 32 this method does not require dual-frequency measurements for mass determination, only
 33 validation, it can be applied in the future to observations made by many single-frequency
 34 radar systems.

35 **Plain Language Summary**

36 The material left behind as meteoroids burn up in the upper atmosphere has sig-
 37 nificant effects on atmospheric chemistry and dynamics. However, the amount of mass
 38 deposited by any single meteoroid, and therefore the overall input rate, is difficult to cal-
 39 culate. We present a new method for determining individual meteor masses using radar
 40 observations and numerical simulations. We use a physics-based model of the meteor plasma
 41 distribution to simulate the interaction between a radar pulse and a meteor, and calcu-
 42 late observable quantities. Using these simulations, we relate the radar observations to
 43 physical characteristics of the meteor, which we then use to estimate the mass. Since this
 44 method only requires a single radar observation to calculate a meteor's mass, we apply
 45 it to a set of meteors observed at the same time by two radar systems, and compare the
 46 results.

47 1 Introduction

48 As a meteoroid travels through an atmosphere it undergoes a process called abla-
 49 tion in which its outer layers are converted into a plasma, primarily due to frictional heat-
 50 ing and sputtering. The vast majority of meteoroids that enter the atmosphere are ex-
 51 tremely small, on the order of mg to μg (Flynn, 2002), and most of them ablate entirely.
 52 Most meteoroids ablate between 80 and 120 km altitude (Ceplecha et al., 1998; Kero et
 53 al., 2012; Schult et al., 2017; Janches et al., 2015). Metallic ions originating from the me-
 54 teoroid itself deposited in this region interact with the existing E-region ionospheric plasma
 55 population in various ways. The input of meteoric material can cause the formation of
 56 metal layers, change ionospheric conductivities, densities, and compositions, and seed
 57 the formation of high-altitude clouds (Plane, 1991; Ellyett & Kennewell, 1980; Rosin-
 58 ski & Pierrard, 1964). However, the mass of any single meteoroid, and therefore the amount
 59 of mass it deposits in the atmosphere during ablation, is difficult to determine with suf-
 60 ficient precision. As a result the total meteoric mass flux is poorly constrained, with es-
 61 timates ranging from 5 to more than 250 tons per day (Plane, 2012). Each estimate de-
 62 pends on the method of observation, the process used to determine individual masses,
 63 and the assumed size and velocity distribution of the meteoroid population. Each step
 64 incorporates numerous assumptions about the physical processes involved. Additionally,
 65 meteoroids occur in an extremely broad range of sizes, and no single technique can ob-
 66 serve the entire distribution. For example, meteor radars readily observe small particles
 67 over a large range of masses, ng-mg, while optical camera networks can only detect par-
 68 ticles on the order of a mg or larger (ReVelle, 2003; Schult et al., 2017, 2020; Stober et
 69 al., 2011; Janches et al., 2014). Optical observations thus neglect the numerous μg -sized
 70 meteoroids, while the statistical occurrence of larger meteoroids in radar meteor data
 71 is low compared to the occurrence of small and moderately sized particles. Other tech-
 72 niques measure mass more directly, such as analysis of cratering on satellite-based de-
 73 tectors, but have selection biases based on the velocity of incoming particles (Love & Brown-
 74 lee, 1993). Hunt et al. (2004) showed that high-gain radars also have a velocity bias, and
 75 preferentially detect large, fast meteoroids.

76 The plasma that makes up a meteor consists of two parts: the dense plasma that
 77 forms around the meteoroid as it ablates, called the head plasma, and the diffuse plasma
 78 left behind, called the trail. High-power large aperture (HPLA) radar systems readily
 79 detect the head plasma of meteors, and have been used to do so for decades (McKinley

& Millman, 1949). Radar cannot detect the plasma density directly, but instead measure the radar cross section (RCS). The observed RCS depends on the shape, physical extent, and density of the meteor plasma distribution, as well as its location within the radar beam and the radar frequency. Various techniques can also be used to measure the meteor's velocity and spatial location (Elford et al., 1995; Steel & Elford, 1991; Mazur et al., 2020). In this work we will address the difficulty of converting radar observations of head plasmas into mass estimates and introduce a method that uses results from computer simulations to determine individual masses.

Meteor masses can be inferred from observations ("mass inversion") using various techniques, though the reliability of any given method is difficult to ascertain. Radar mass inversion techniques rely on determining the relationship between observable parameters (primarily RCS, velocity, altitude) and the meteor mass. In general, this requires assumptions about the shape of the head plasma and the physical relationships between the observable parameters and electron density in the head plasma. Close et al. (2004) demonstrates a mass inversion method that relates the size of a meteor to its velocity and altitude, then applies a spherical scattering model to convert between RCS and plasma density.

The simulation method used in this work is based on the method introduced in Marshall and Close (2015). Marshall and Close used a finite difference time domain (FDTD) model to simulate the interaction between an incident radar wave and the head plasma of a meteor, then calculated the RCS that radar systems with various transmission frequencies would observe for a meteor of given size and shape parameters. The FDTD method is discussed in greater detail in Section 3.1.

Marshall and Close (2015) used a simple, spherically symmetric 3D Gaussian model to describe the meteor head plasma. Since this model has two free parameters and only a single measurement (RCS), dual-frequency observations are required to uniquely determine the mass. In this work, we incorporate a physics-based model for the meteor head plasma. This model uses radar-measurable parameters including velocity and altitude to define the distribution, requiring fewer assumptions about the structure of the plasma and allowing masses to be derived from a single radar measurement, instead of the dual-frequency method described in Marshall and Close. This plasma model incorporates a more physical description of the meteor plasma, and allows the mass inversion scheme

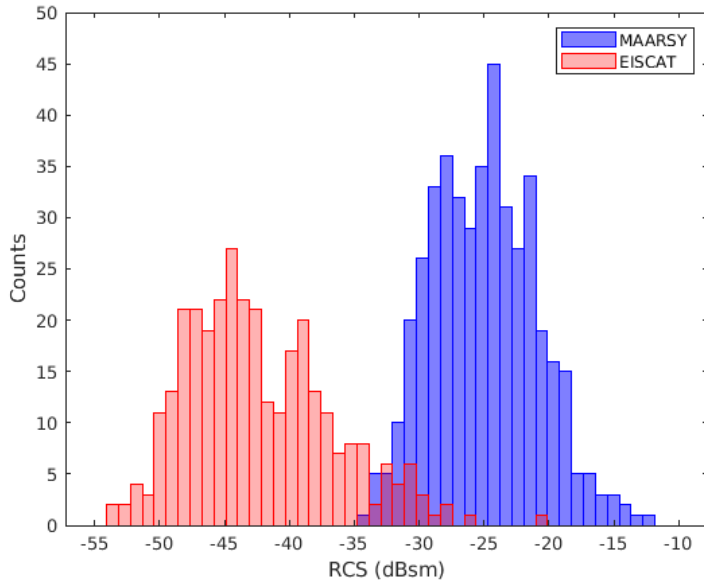


Figure 1. Histograms of the median RCS for each radar profile for MAARSY (blue) and EISCAT (red).

to be applied to any single-frequency set of radar observations, rather than requiring dual-frequency observations. To test and validate this new approach, we apply our method to a set of dual-radar meteor observations, described in the following section. The dual-frequency observations allow the method to be independently validated using coincident meteor observations.

2 Data

The radar data used in this work consists of 485 meteors that were observed coincidentally by MAARSY (53.5 MHz) and EISCAT (929 MHz) radars in Norway between 30 September 2016 and 25 March 2017. Figure 1 shows histograms of the observed RCS values for both radars. In general, the MAARSY RCS values are higher than the EISCAT values by an average of 16.7 dB. EISCAT has a narrow beam width (0.7° HPBW) compared to MAARSY (3.6° HPBW), so most meteors are observed for a longer period with MAARSY than with EISCAT. The narrow beam also restricts the altitudes at which both radars can observe a meteor at the same time to a limited range (90–110 km). The dataset and observation techniques are described in detail in Schult et al. (2021).

127 Figure 2 shows three example radar profiles of RCS versus time for observed me-
 128 teors. The dotted lines indicate the coincident region, during which both radars observed
 129 the meteor at the same time. Panel a.) shows a smooth, well-behaved observation. Panel
 130 b.) shows a case with some large spikes in the EISCAT observation. Panel c.) shows a
 131 case with significant gaps in the MAARSY observation, and in which the coincident re-
 132 gion consists of only a few observation points. While we attempt to estimate a mass for
 133 every observation, cases such as those in panels b.) and c.) can lead to unreliable esti-
 134 mates or fall outside of the simulated parameter space. In the case of gaps in the data,
 135 we use a linear interpolation to fill in the missing points.

136 The spikes in the EISCAT data are formed when the meteor target passes a min-
 137 imum in the narrow EISCAT UHF antenna radiation pattern. There, the antenna gain
 138 changes fast as a function of position and the true gain of the antenna differs from the
 139 ideal radiation pattern of a Cassegrain antenna used to convert the measured SNR to
 140 RCS (see Kero et al. (2008)). A mitigation method to avoid these spikes might be to re-
 141 place RCS values where the antenna gain is lower than a certain threshold with a lin-
 142 ear interpolation, as in the case of missing data points. However, testing has shows that
 143 the mass estimates for profiles with such artefacts are similarly distributed to those for
 144 smooth profiles, and do not produce higher than expected masses. While one might ex-
 145 pect that a large artificial spike in RCS would correspond to an increase in the estimated
 146 mass, in such cases the data is unphysical and falls outside of the parameter space of the
 147 analysis (described in the following section), and thus does not contribute to the mass
 148 estimate. In this case we choose to use the original RCS profiles without replacing any
 149 of the data, as doing so does not seem to introduce any bias or artificial inflation to the
 150 mass estimates.

151 3 Methodology

152 The mass inversion method presented in this work requires finite difference time
 153 domain (FDTD) simulations to relate observed RCS profiles to physical plasma distri-
 154 butions. In this section we describe the FDTD model, the steps of the mass inversion
 155 scheme, and the treatment of uncertainty.

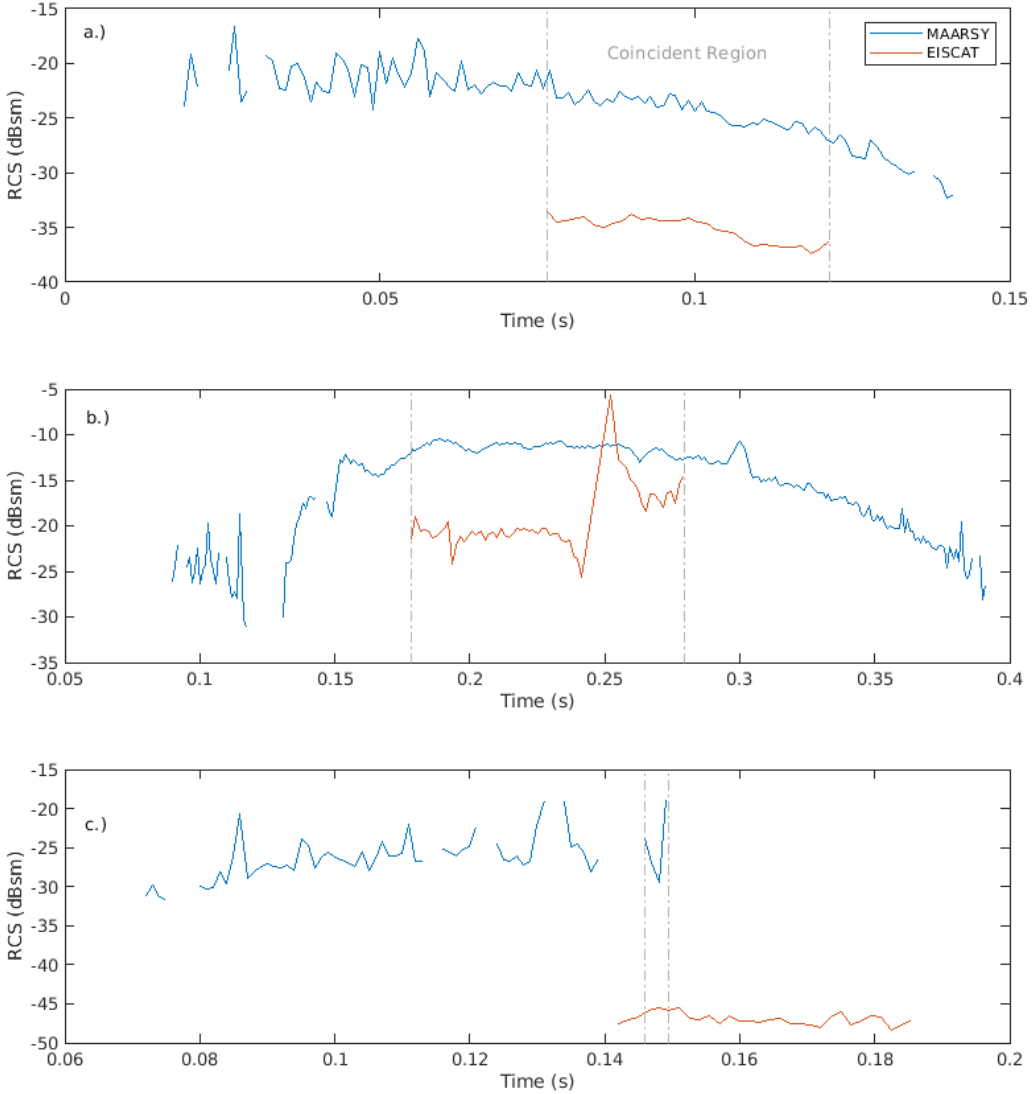


Figure 2. Example RCS profiles. The coincident region, where both radar observe the meteor at the same time, is marked by dashed lines. Many profiles are smooth (a.), but some have sudden large spikes or troughs (b.), significant gaps in the observation, or are only observed coincidentally at a few points (c.).

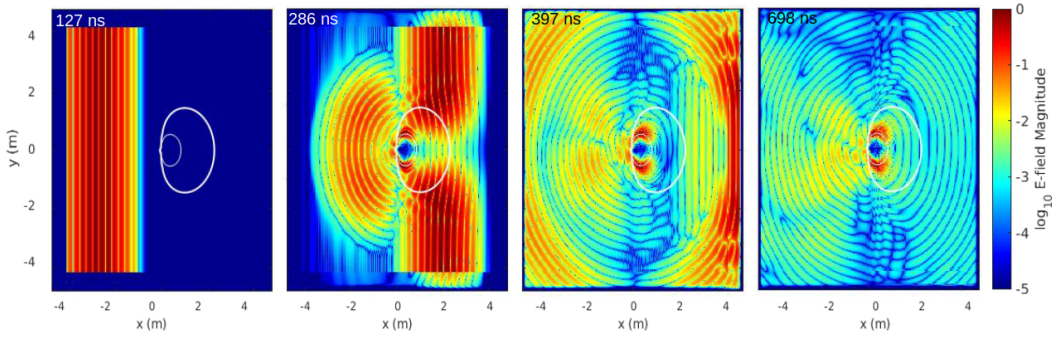


Figure 3. Snapshots from an FDTD simulation. The simulated radar pulse enters the box from the left (panel 1) and interacts with the meteor plasma, represented by the white contour lines (panel 2). The thin inner line represents the overdense area, or the region in which the plasma frequency ω_p is greater than the transmitted frequency ω ($\omega_p \geq \omega$). The thick outer line represents the region in which the plasma frequency is a factor of e less than the transmitted frequency, ($\omega_p \leq \omega/e$). Some portion of the pulse reflects from the plasma (panel 3), leaving small-scale perturbations behind (panel 4).

156

3.1 FDTD Model

157

158

159

160

161

162

163

164

165

166

167

The FDTD simulations in this work are based off of those in Marshall and Close (2015), which describes the method in detail. The model simulates a radar pulse encountering and scattering from a static plasma distribution. As the total length of a single simulation is on the order of a few microseconds, it is reasonable to assume that the meteor plasma is stationary for the duration of a single radar pulse. The model solves Maxwell's equations in a cold, collisional, magnetized plasma, according to the standard FDTD algorithm presented in Yee (1966). The RCS is estimated using a total-field / scattered-field method near the meteor (within the simulation box), which is mapped to the far field using a near-to-far-field transformation (Inan & Marshall, 2011). Figure 3 shows a sequence of stills from a simulation, showing the radar pulse before encountering the meteor plasma (left) and during and after the scattering of the pulse from the plasma.

168

169

170

171

172

Marshall and Close used this method to simulate observations at several frequencies of meteors of various sizes with a 3D Gaussian distribution of plasma density. The meteors were defined by a peak density and a size scale parameter, leading to a system with two unknowns and one measurement (RCS). They suggest that the solution is to combine two simultaneous observations of the same meteor at different frequencies. By

173 implementing a different plasma distribution, we avoid this problem, and can estimate
 174 the meteoroid mass using a single frequency observation.

175 Dimant and Oppenheim (2017) presented a new model for the head plasma of a
 176 meteor derived using kinetic theory. The model is built from a first-principals analysis
 177 of the plasma formed around a small meteoroid as it travels through an atmosphere, and
 178 describes the head plasma at a single instant in time. The density falls off from a peak
 179 around the source location roughly exponentially ahead of the meteor, as $1/r^2$ behind
 180 it, and as $1/r^3$ perpendicular to the path. Figure 4 shows an example of the Dimant-
 181 Oppenheim (DO hereafter) distribution, with relevant density contours. The distribu-
 182 tion is fully defined by four parameters: the source meteoroid's radius (r_M), altitude (h),
 183 and velocity (U), as well as a plasma density parameter (n_0). The radius and density
 184 parameters appear together as a coefficient $n_0 r_M^2$ which cannot be separated in the fol-
 185 lowing analysis, so we treat the product as a single size parameter. Crucially, this allows
 186 us to uniquely define a plasma distribution in terms of three variables, two of which (ve-
 187 locity and altitude) are directly measurable with a radar. By adopting this plasma dis-
 188 tribution we have moved from a problem with two unknowns and one measurement to
 189 one with three unknowns ($n_0 r_M^2$, h , and U) and three measurements (RCS, h , and U),
 190 a solvable system.

191 In the following analysis, we use data from simulations at four altitudes (95–110
 192 km). At each altitude and for each radar, 750 unique meteors were simulated spanning
 193 twenty five velocities (20–70 km/s), and 30 size parameters ($n_0 r_M^2 = 10^{12.4}–10^{14.4}$ m⁻¹).
 194 The altitude and velocity parameter ranges were chosen based on the physical occurrence
 195 of meteors; the size parameter range was chosen such that the simulated RCS values cover
 196 the range of observed values. The general trends in RCS with each parameter are as fol-
 197 lows: strong linear increase in RCS (dB) with logarithmically increasing size parame-
 198 ter; weak, approximately linear decrease in RCS with linearly increasing altitude; and
 199 weak RCS dependence on velocity, with a peak in RCS around 25 km/s. Figure 5 shows
 200 the 100 km altitude lookup tables for each radar system. Note that for any given set of
 201 parameters, the FDTD model predicts that MAARSY will observe an RCS that is 20–
 202 30 dB greater than EISCAT observes, a difference that is similar but somewhat larger
 203 than that observed in the MAARSY/EISCAT coincident dataset described in Section 2.

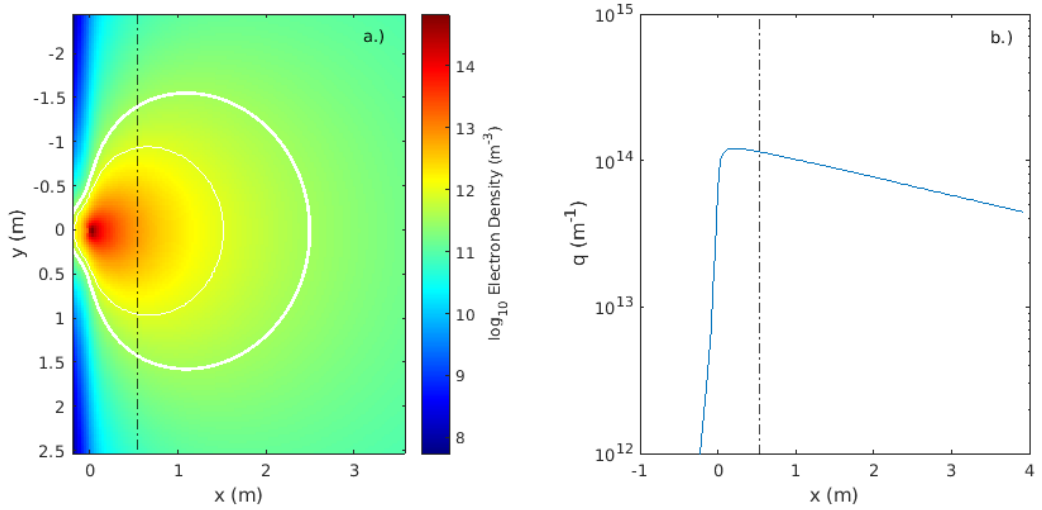


Figure 4. Example of the Dimant-Oppenheim head plasma distribution, for a meteor at 100 km travelling at 60 km/s (a.). Contours are the same as in Figure 3. The location in the tail at which the line density q is calculated is shown by the black dashed line. The value of q at each grid location is shown on the right (b.).

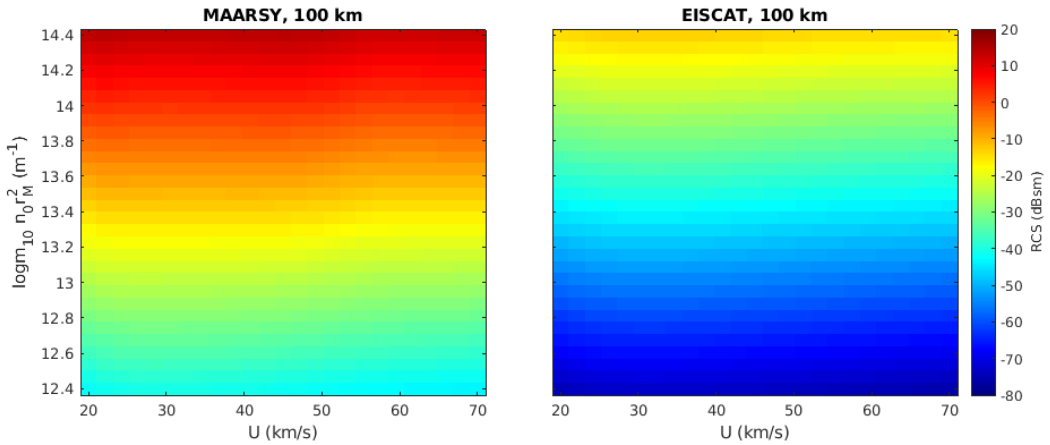


Figure 5. MAARSY (left) and EISCAT (right) lookup tables at 100 km.

204 **3.2 Mass inversion scheme**

205 Once the lookup tables have been created, they are used to invert radar observations
 206 to estimate masses. For each time step within a single observation, the scheme is:

- 207 1. Use the appropriate lookup table to determine the size parameter $n_0 r_M^2$ from the
 observed altitude, velocity, and RCS.
- 209 2. At each timestep, the DO distribution is now fully defined by the observed altitude,
 observed velocity, and inferred size parameter. Generate this full head plasma
 distribution and use it to calculate the line density q .
- 212 3. Use q to calculate the mass loss rate $\frac{dm}{dt}$ and integrate over the full observation
 to estimate the mass m .

214 The lookup tables are defined for a discrete parameter space. In the (likely) event
 215 that the observed parameters do not exactly equal the simulated parameters, we linearly
 216 interpolate the tables to the observed values. First, the two tables nearest in altitude to
 217 the observation are used to interpolate to the observed altitude. Next, this table is in-
 218 terpolated to the observed velocity. Finally, a linear fit in log-log space is applied to the
 219 resulting data (RCS as a function of $n_0 r_M^2$) and inverted to estimate the size parame-
 220 ter. This estimate, together with the observed altitude and velocity, constitute the as-
 221 sumed plasma distribution of the meteor at the observation timestep.

222 The spacing of the simulated data was chosen to minimize the error introduced by
 223 this linear interpolation, such that this error is small compared to other sources of un-
 224 certainty, described later. An exception to this claim is when the observed RCS falls within
 225 the Mie scattering regime. At large values of the size parameter, the meteors enter the
 226 Mie scattering regime at MAARSY's frequency of 53 MHz. In this case the relationship
 227 between RCS and meteor size is non-linear, and a unique inversion does not exist. While
 228 few of the observed meteors appear to fall within this regime, the linear fit can lead to
 229 over- or under-estimations of mass for large meteors. This is not an issue for the EIS-
 230 CAT simulations, as at all simulated sizes the meteors are within the Rayleigh scatter-
 231 ing regime.

232 Once the distribution is defined, the line density q is calculated numerically by in-
 233 tegrating the density in a slice through the region in the wake of the meteor. This in-
 234 tegration is numeric, not analytic, and has some variation depending on the exact loca-

235 tion selected (Figure 4b). The line density can be thought of as the amount of ioniza-
 236 tion produced by the meteoroid per unit length along its trajectory.

237 This process is repeated at each timestep in the observation, building an array of
 238 q as a function of time. The line density is related to the total mass lost by the meteor
 239 at a single moment (dm/dt) by the velocity U , species mass μ , and the ionization effi-
 240 ciency β . The total mass estimate is defined by the integral (Close et al., 2004):

$$m = \int_{t_1}^{t_2} \frac{q U \mu}{\beta} dt \quad (1)$$

241 In the following analysis, we assume a species mass of $\mu = 5.12 \times 10^{-26}$ kg, based
 242 on a composition of 70% oxygen and 30% silicon, and corresponding to a mass density
 243 of 700 kg/m³. We also assume the ionization profile for iron derived in DeLuca et al. (2018),
 244 $\beta = 2.49 \times 10^{-4} v [\text{km/s}]^{2.04}$. This profile is the result of laboratory experiments. While
 245 the assumed composition does not include iron, we have adopted the DeLuca et al. (2018)
 246 result on the assumption that this velocity-dependent model improves on the assump-
 247 tion of a constant ionization efficiency for all meteors at all speeds, and there are no doc-
 248 umented β measurements for oxygen/silicon. The implications of these assumptions are
 249 discussed in Section 5.

250 The bounds of integration are chosen based on the desired mass product. For the
 251 purpose of comparison between MAARSY and EISCAT only the mass lost in the coinci-
 252 dent region (the “coincident mass”) should be considered, so the integral is taken only
 253 over the time that both radar observe the meteor. To determine the total mass of the
 254 meteoroid, the integral is taken over the entire observation.

255 3.3 Sources of uncertainty in modeling and fitting

256 The choice of numerical parameters in the FDTD simulation space leads to numer-
 257 ical errors and uncertainty in the estimated RCS values. To quantify these errors, we have
 258 run extensive test simulations over simulation parameters and estimated the variation
 259 of the resulting RCS. Capturing the relevant physics requires both that the meteor plasma
 260 fit entirely within the simulation box, and that the grid size is small enough to resolve
 261 both the radar wavelength and the plasma distribution. As the radar pulse enters the
 262 dense head plasma the wavelength shrinks, compounding this problem. Even when the

grid size is sufficiently small as to well-resolve the meteor, there is some variation in the calculated RCS as the grid size changes. After running multiple simulations varying the grid size parameter, we found the variation in RCS due to this factor to be ± 2 dB. Because the analytic distributions used to define a meteor in the simulation are not hard targets but fall off asymptotically at the edges, it is impossible to define a simulation box that encompasses it entirely. However, the plasma density falls off sufficiently quickly at the edges that as long as the box is “sufficiently” large (determined experimentally), there is no variation in RCS with changing box size. The linear fit used to create the lookup tables described above adds an additional RMS error of 0.4 dB. The actual error is larger in the Mie regime; however, the dataset includes few meteors large enough to fall into the Mie regime. Finally, the total runtime of the simulation also causes some variation in RCS, but as long as the simulation is run long enough to capture the initial reflection of the pulse this variation is small (0.05 dB). The total error in RCS associated with all of these aspects of the FDTD model is about 2.5 dB. While other sources of error certainly exist, we believe that they are small in magnitude compared to those enumerated here. These errors are carried through the analysis and are used to calculate errors on the resulting mass distributions.

4 Results

The process described in Section 3 was applied to a set of 485 radar observations, as described in Section 2. After removing observations for which there is no coincident region or for which no mass could be determined using this method, we produce mass estimates for 271 meteors. For each individual meteor, independent mass estimates were calculated using the MAARSY and EISCAT observations, since as described above, this method requires only a single-frequency RCS measurement. Figure 6 shows a scatter plot of the EISCAT estimate plotted against the MAARSY estimate, with 1σ error bars. Note that these estimates are only of the mass produced in the coincident region. The sources and propagation of error are described in Section 3. In the coincident region, the EISCAT mass estimate is typically slightly higher than the MAARSY estimate, but there is a strong linear correlation between the two.

In general, the mass estimation scheme performs well. A linear fit in log-log space to the calculated masses (see Figure 6) shows that on average, there is a factor of 1.33 difference between the estimates, and that there is a strong linear correlation between

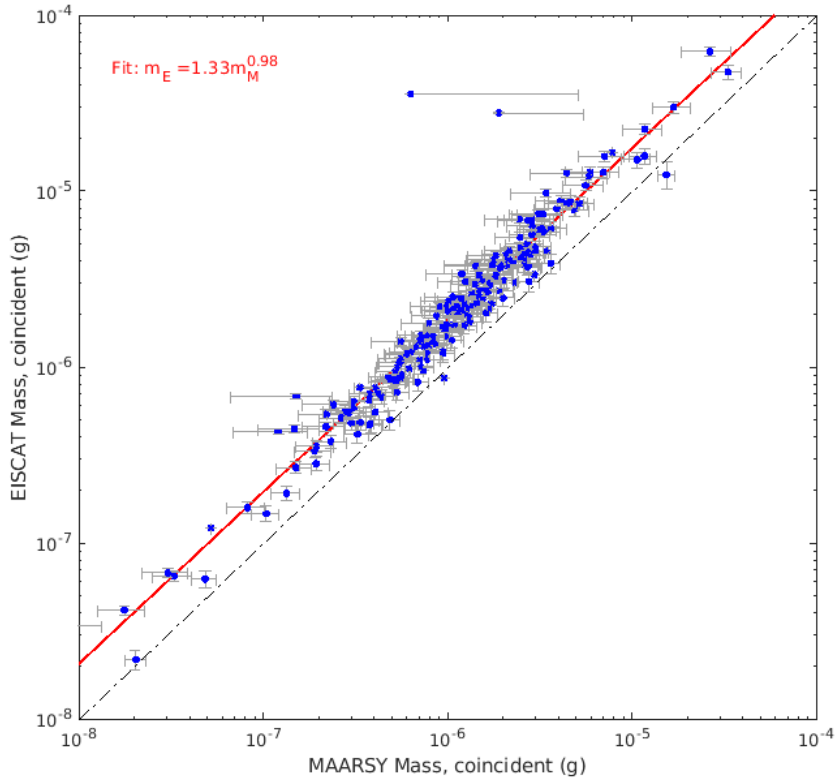


Figure 6. Masses estimated using EISCAT vs. MAARSY data, with 1σ error bars. The black dashed line represents exact equality. The red line represents a linear fit in log-log space, neglecting outliers. The fit shows that there is a strong linear correlations between the two estimates, but that the EISCAT estimates are on average a factor of 1.33 greater than the MAARSY estimates.

them. However, the source of this disparity is not yet understood, as it may arise from a number of possible sources. We discuss the offset in this plot and possible sources of the discrepancy in Section 5.

The individual mass estimates can be combined to describe the mass distribution observed by both radars. The left panel in Figure 7 shows the distributions of the total meteor mass, and the right panel shows the mass lost in the coincident region. The total mass distributions show that the MAARSY distribution (median: $38 \mu\text{g}$) peaks more than an order of magnitude higher than the EISCAT distribution (median: $2.3 \mu\text{g}$). This result is as one might expect, given that MAARSY has a significantly larger beamwidth

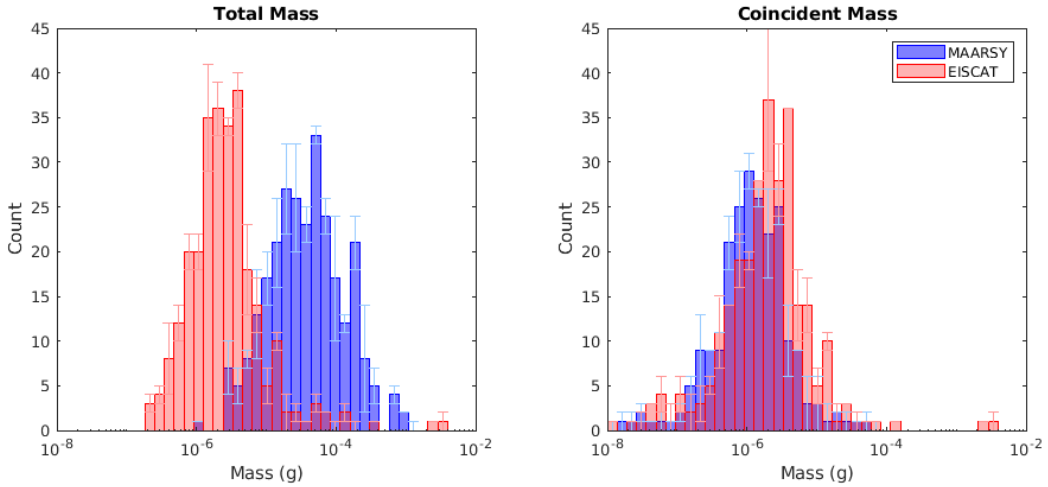


Figure 7. Mass distributions for total observations (left) and coincident observations (right), with 1σ error bars.

and observes a larger volume than EISCAT. Typically, meteors are observed for a longer duration by MAARSY due to the larger beamwidth, hence the total mass is integrated over a longer trajectory. 80% of the MAARSY masses lie between 7.7 and 192 μg ; 80% of the EISCAT masses lie between 0.68 and 10 μg .

The total mass distributions are of significant scientific interest, particularly the MAARSY distribution, which captures a larger portion of the meteor trail, but they provide little insight into the validity of this method. As a validation check, we consider the coincident region masses, which include only the mass lost during the period when both radars are observing the meteor. The EISCAT and MAARSY masses are calculated using independent observations and simulations, so good agreement between them provides confidence in our inversion method. We see from Figure 6 that there is a strong linear relationship between the two estimates, with several outliers clustered at high masses. Note that in almost all cases, the EISCAT mass estimate is greater than the MAARSY estimate. Figure 7 (right) shows the corresponding mass distributions. In this case, the EISCAT distribution peaks at slightly higher mass than the MAARSY distribution, again indicating that the EISCAT estimates are more massive than the MAARSY estimates. Possible sources for this disparity are addressed in Section 5. However, the two distributions show reasonable agreement over the whole dataset.

322 **5 Discussion and Conclusions**

323 This paper presents a method for combining radar observations with the results
 324 of FDTD modeling to produce meteor mass estimates. Lookup tables produced from FDTD
 325 simulations relating a theoretical plasma distribution to a radar cross section are used
 326 to map radar observations of altitude, velocity, and RCS to line densities, which are then
 327 integrated to estimate masses. This method enables the estimate of meteor masses from
 328 a single-frequency radar observation. The procedure is applied to several hundred me-
 329 teors observed coincidentally by the EISCAT and MAARSY radars, and the masses cal-
 330 culated using both sets of data are compared.

331 While we have reduced the number of assumptions used to calculate masses where
 332 possible, some remain. In Equation 1, the ablated species mass μ and the ionization ef-
 333 ficiency β must be specified. We have assumed a mixture of oxygen and silicon in this
 334 analysis; however, since the mass is linearly proportional to the species mass, changing
 335 the assumed μ simply scales the resulting masses. The ionization efficiency profile from DeLuca
 336 et al. (2018) is experimentally derived and is a function of velocity, rather than a con-
 337 stant value for all meteors. Mass is inversely proportional to the ionization efficiency, so
 338 adjusting β also linearly scales the mass. The resulting mass distributions are in reason-
 339 able agreement with past measurements. Close et al. (2004) derived masses on the or-
 340 der of $10^{-9} - 10^{-1}$ g using UHF and VHF radar observations and assuming Gaussian
 341 density profiles. Using the same dataset as this work, (Schult et al., 2021) derived masses
 342 ranging from $10^{-7} - 10^{-2}$ g, again assuming a Gaussian distribution and using a dual-
 343 frequency technique.

344 The choice of where in the meteor tail to calculate the line density also introduces
 345 some variation. As shown in Figure 4b, the line density is negligible in front of the me-
 346 teoroid, rises sharply and peaks at the meteoroid center, then decays slowly down the
 347 tail. Theoretically, one would expect that the line density would be constant in the tail,
 348 as the ionization produced at the meteoroid is all left in the trail, where it neither in-
 349 creases nor decreases. However, as the bounds of the numerical integration must be fi-
 350 nite and the distribution approaches 0 only asymptotically, some of the density distri-
 351 bution lies outside of the box. The amount of particles outside the box should increase
 352 with distance from the meteoroid, as the plasma expands, which would explain the shape
 353 of Figure 4b. Further investigation has shown that doubling the box size while maintain-

354 ing the size of the meteor increases the peak value of q less than 5%, indicating that most
 355 of the density is captured within the bounds of integration. In accordance with this ex-
 356 planation, we have chosen to calculate q just behind the meteoroid, with the goal of cap-
 357 turing as much of the distribution as possible.

358 As shown in Section 4 above, the masses estimated using EISCAT data are on av-
 359 erage 1.33 times larger than those estimated using MAARSY data. A clue to this dis-
 360 crepancy is found in the difference between the MAARSY and EISCAT RCS values. Fig-
 361 ure 8 compares the difference between the median MAARSY and EISCAT RCS for a
 362 given head echo and the expected difference based on the FDTD model. There is a wide
 363 spread in the RCS differences in the data, but on average the difference is 15–20 dB. How-
 364 ever, the FDTD model predicts RCS differences on the order of 30 dB. The model pre-
 365 dicts a spread of 2–3 dB in the RCS difference due to variation in altitude and velocity,
 366 but does not reproduce the more than 20 dB spread observed in the data. It is not clear
 367 whether the model is over estimating MAARSY RCS values, under estimating EISCAT
 368 RCS values, or if some of the disparity can be attributed to the RCS calculations in the
 369 radar data. Uncertainty in the radar gain patterns and pointing may account for 3–5 dB;
 370 however these uncertainties are not sufficient to explain the 10 dB shift. The FDTD model
 371 predicts that with increasing MAARSY RCS, a proxy for the size of the meteor, the RCS
 372 difference between the two radars decreases ($\Delta\text{RCS} \propto -0.077 \cdot \text{RCS}$); this trend is also
 373 observed in the data ($\Delta\text{RCS} \propto -0.104 \cdot \text{RCS}$). Repeating the analysis with EISCAT RCS
 374 values artificially decreased by 10 dB reduces the offset between the MAARSY and EIS-
 375 CAT masses from a factor of 1.33 to 1.05.

376 A possible source of the difference between the simulated and observed RCS dif-
 377 ferences is the aspect angle, or the angle between the radar pulse and the meteor's di-
 378 rection of motion. The FDTD simulations used to create the lookup tables all assume
 379 that the meteor is travelling directly toward the radar. However, the radars do not nec-
 380 essarily or even probably observe meteors with this viewing geometry. Due to differences
 381 in pointing direction, MAARSY observes more meteors close to head-on, while EISCAT
 382 is more likely to point close to perpendicular to the trail. Test simulations show that the
 383 RCS decreases slightly (1–2 dB) when the aspect angle is shifted by 90°, but not enough
 384 to explain the full 10 dB discrepancy. The simulations also show that EISCAT is more
 385 sensitive to aspect angle than MAARSY; rotating the meteor 90° from pointing directly

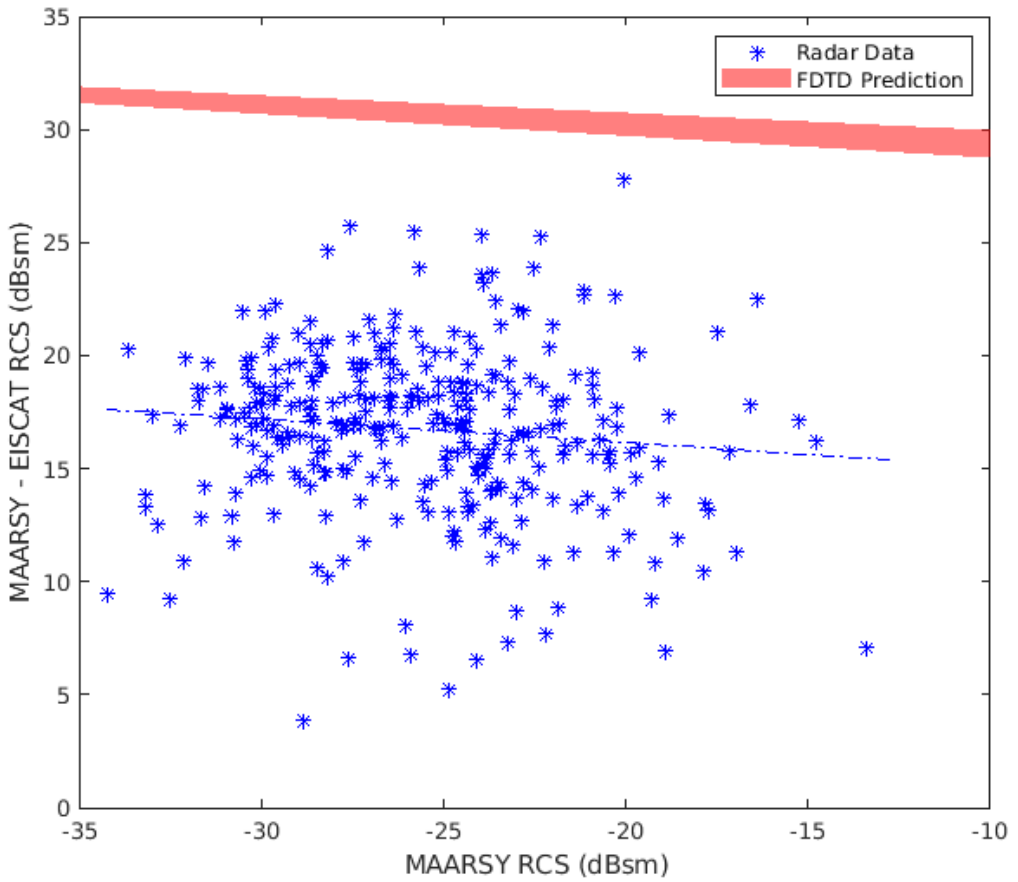


Figure 8. RCS difference between MAARSY and EISCAT observations, as predicted by the FDTD model (red) and in the data (blue). A linear fit to the radar data is shown by the blue dashed line.

386 at the radar to perpendicular to the beam shifts the RCS by 0.88 dB for MAARSY and
 387 1.99 dB for EISCAT.

388 Kero et al. (2008) used the three EISCAT UHF receivers to compare the mono-
 389 static RCS of a meteor target with two simultaneously probed bistatic RCSs at differ-
 390 ent aspect angles. Meteoroids from all possible directions entering the common volume
 391 monitored by the three receivers were detected, out to an aspect angle of 130° from the
 392 meteoroid trajectories. The RCS of individual meteors as observed by the three receivers
 393 were equal within the accuracy of the measurements, which is consistent with an essen-
 394 tially isotropic scattering process as had previously been inferred from polarization mea-
 395 surements by Close et al. (2002). The results of the simulations presented here indicate
 396 that aspect angle might play a more significant role than previously thought, particu-
 397 larly when comparing observations from radar of different frequencies. We intend to in-
 398 vestigate the importance of the aspect angle in future work, as well as the effects of frag-
 399 mentation.

400 As discussed in Section 3.3, we have propagated all sources of error that we could
 401 constrain in this analysis. On the modeling side, these include variation in the grid size,
 402 the box size, and the total duration of the simulation. Where possible, model param-
 403 eters were chosen to minimize these errors. We also include error due to the interpola-
 404 tion and fitting involved in the process of determining the size parameter. When prop-
 405 agated through the analysis, the resulting mass error due to FDTD simulation errors is
 406 in general about 10%. We do not include uncertainties in the radar measurements in this
 407 analysis.

408 The ultimate goal of developing this method is to apply it broadly in order to es-
 409 timate the total mass flux and mass distribution entering the Earth's atmosphere. While
 410 dual frequency measurements are required for the verification and comparison performed
 411 in this work, the general method requires only a single frequency. It can thus be used
 412 on datasets from many radar systems at various frequencies, although modeling constraints
 413 currently restrict the FDTD simulations to frequencies less than 1 GHz. However, this
 414 limitation is due to constraints on computer resources used by the FDTD simulations,
 415 and could be overcome by increasing the parallelization of the FDTD code or improved
 416 computing power.

417 **Acknowledgments**

418 This work was supported by National Science Foundation awards 1833209 and 1754895,
 419 and utilized resources from the University of Colorado Boulder Research Computing Group,
 420 which is supported by the National Science Foundation (awards ACI-1532235 and ACI-
 421 1532236), the University of Colorado Boulder, and Colorado State University. The au-
 422 thors thank Carsten Schult from IAP for his enthusiasm performing the data analysis for
 423 MAARSY. Gunter Stober and Carsten Schult were supported by grant STO 1053/1-1
 424 (AHEAD) of the Deutsche Forschungsgemeinschaft (DFG). We are grateful to IAP col-
 425 leagues Ralph Latteck and J. L. Chau for keeping MAARSY operational during the cam-
 426 paign period. We gratefully acknowledge the EISCAT staff for their assistance during
 427 the experiments, and Asta Pellinen-Wannberg who took an active part in the initial plan-
 428 ning. EISCAT is an international association supported by research organizations in China
 429 (CRIPR), Finland (SA), Japan (NIPR and ISEE), Norway (NFR), Sweden (VR), and
 430 the United Kingdom (UKRI). Johan Kero was supported by the Swedish Research Coun-
 431 cil, Sweden, Project Grant 2012-4074 to carry out the EISCAT radar experiments and
 432 initial data analysis. The FDTD lookup tables and processing code used in this anal-
 433 ysis are available on Zenodo at <http://doi.org/10.5281/zenodo.4723667>. The radar data
 434 is available on Zenodo at <http://doi.org/10.5281/zenodo.4731084>.

435 **References**

- 436 Ceplecha, Z., Borovička, J., Elford, W., ReVelle, D. O., Hawkes, R. L., Porubčan, V.,
 437 & Šimek, M. (1998). Meteor phenomena and bodies. *Space Science Reviews*.
 438 doi: 10.1023/A:1005069928850
- 439 Close, S., Oppenheim, M., Hunt, S., & Coster, A. (2004). A technique for cal-
 440 culating meteor plasma density and meteoroid mass from radar head echo
 441 scattering. *Icarus*, 168(1), 43 - 52. doi: 10.1016/j.icarus.2003.11.018
- 442 Close, S., Oppenheim, M., Hunt, S., & Dyrud, L. (2002). Scattering characteristics
 443 of high-resolution meteor head echoes detected at multiple frequencies. *Journal*
 444 *of Geophysical Research: Space Physics*, 107(A10), SIA 9-1-SIA 9-12. doi: 10
 445 .1029/2002JA009253
- 446 DeLuca, M., Munsat, T., Thomas, E., & Sternovsky, Z. (2018). The ionization ef-
 447 ficiency of aluminum and iron at meteoric velocities. *Planetary and Space Sci-*
 448 *ence*, 156, 111-116. (Dust, Atmosphere, and Plasma Environment of the Moon

- 449 and Small Bodies) doi: 10.1016/j.pss.2017.11.003
- 450 Dimant, Y. S., & Oppenheim, M. M. (2017). Formation of plasma around a small
451 meteoroid: 2. implications for radar head echo. *Journal of Geophysical Re-*
452 *search: Space Physics*, 122(4), 4697-4711. doi: 10.1002/2017JA023963
- 453 Elford, W. G., Cervera, M. A., & Steel, D. I. (1995). Meteor Velocities: A New Look
454 at an Old Problem. *Earth Moon and Planets*, 68(1-3), 257-266. doi: 10.1007/
455 BF00671514
- 456 Ellyett, C., & Kennewell, J. (1980). Radar meteor rates and atmospheric density
457 changes. *Nature*, 287. doi: 10.1038/287521a0
- 458 Flynn, G. J. (2002). Extraterrestrial dust. In E. Murad & I. P. Williams (Eds.), *Me-*
459 *teors in the earth's atmosphere*. Cambridge: Cambridge University Press.
- 460 Hunt, S., Oppenheim, M., Close, S., Brown, P., McKeen, F., & Minardi, M. (2004).
461 Determination of the meteoroid velocity distribution at the earth using high-
462 gain radar. *Icarus*, 168(1), 34-42. doi: 10.1016/j.icarus.2003.08.006
- 463 Inan, U. S., & Marshall, R. A. (2011). *Numerical electromagnetics: The fdtd method*.
464 Cambridge University Press. doi: 10.1017/CBO9780511921353
- 465 Janches, D., Plane, J. M. C., Nesvorný, D., Feng, W., Vokrouhlický, D., & Nicolls,
466 M. J. (2014). Radar Detectability Studies of Slow and Small Zodiacal Dust
467 Cloud Particles. I. The Case of Arecibo 430 MHz Meteor Head Echo Observa-
468 tions. *Astrophysical Journal*, 796(1), 41. doi: 10.1088/0004-637X/796/1/41
- 469 Janches, D., Swarnalingam, N., Plane, J. M. C., Nesvorný, D., Feng, W., Vokrouh-
470 lický, D., & Nicolls, M. J. (2015). Radar Detectability Studies of Slow and
471 Small Zodiacal Dust Cloud Particles: II. A Study of Three Radars with Differ-
472 ent Sensitivity. *Astrophysical Journal*, 807(1), 13. doi: 10.1088/0004-637X/
473 807/1/13
- 474 Kero, J., Szasz, C., Nakamura, T., Meisel, D. D., Ueda, M., Fujiwara, Y., ...
475 Watanabe, J. (2012). The 2009–2010 MU radar head echo observation pro-
476 gramme for sporadic and shower meteors: radiant densities and diurnal rates.
477 *Monthly Notices of the Royal Astronomical Society*, 425(1), 135-146. doi:
478 10.1111/j.1365-2966.2012.21407.x
- 479 Kero, J., Szasz, C., Pellinen-Wannberg, A., Wannberg, G., Westman, A., &
480 Meisel, D. D. (2008). Determination of meteoroid physical properties from
481 tristatic radar observations. *Annales Geophysicae*, 26(8), 2217-2228. doi:

- 482 10.5194/angeo-26-2217-2008
- 483 Kero, J., Szasz, C., Wannberg, G., Pellinen-Wannberg, A., & Westman, A. (2008).
484 On the meteoric head echo radar cross section angular dependence. *Geophys.*
485 *Res. Lett.*, 35(7), L07101. doi: 10.1029/2008GL033402
- 486 Love, S. G., & Brownlee, D. E. (1993). A direct measurement of the terrestrial mass
487 accretion rate of cosmic dust. *Science*, 262(5133), 550–553. doi: 10.1126/
488 science.262.5133.550
- 489 Marshall, R. A., & Close, S. (2015). An fdtd model of scattering from meteor head
490 plasma. *Journal of Geophysical Research: Space Physics*, 120(7), 5931-5942.
491 doi: 10.1002/2015JA021238
- 492 Mazur, M., Pokorný, P., Brown, P., Weryk, R. J., Vida, D., Schult, C., ... Agrawal,
493 A. (2020). Precision measurements of radar transverse scattering speeds from
494 meteor phase characteristics. *Radio Science*, 55(10), e2019RS006987. doi:
495 10.1029/2019RS006987
- 496 McKinley, D. W. R., & Millman, P. M. (1949). A phenomenological theory of radar
497 echoes from meteors. *Proceedings of the IRE*, 37(4), 364-375. doi: 10.1109/
498 JRPROC.1949.231641
- 499 Plane, J. (1991). The chemistry of meteoric metals in the earth's upper atmo-
500 sphere. *International Reviews in Physical Chemistry*, 10, 55-106. doi:
501 10.1080/01442359109353254
- 502 Plane, J. (2012). Cosmic dust in the earth's atmosphere. *Chem. Soc. Rev.*, 41, 6507-
503 6518. doi: 10.1039/C2CS35132C
- 504 ReVelle, D. O. (2003). Meteors in the earth's atmosphere: Meteoroids and
505 cosmic dust and their interactions with the earth's upper atmosphere.
506 *Eos, Transactions American Geophysical Union*, 84(26), 249-249. doi:
507 10.1029/2003EO260012
- 508 Rosinski, J., & Pierrard, J. (1964). Condensation products of meteor vapors and
509 their connection with noctilucent clouds and rainfall anomalies. *Journal of At-*
510 *mospheric and Terrestrial Physics*, 26(1), 51 - 66. doi: 10.1016/0021-9169(64)
511 90108-4
- 512 Schult, C., Kero, J., Stober, G., & Brown, P. (2021). Dual frequency measurements
513 of meteor head echoes simultaneously detected with the maarsy and eiscat
514 radar systems. *Icarus*, 355, 114137. doi: 10.1016/j.icarus.2020.114137

- 515 Schult, C., Stober, G., Brown, P., Pokorný, P., & Campbell-Brown, M. (2020).
516 Characteristics of very faint (+16) meteors detected with the middle at-
517 mosphere alomar radar system (maarsy). *Icarus*, 340, 113444. doi:
518 10.1016/j.icarus.2019.113444
- 519 Schult, C., Stober, G., Janches, D., & Chau, J. L. (2017). Results of the first con-
520 tinuous meteor head echo survey at polar latitudes. *Icarus*, 297, 1-13. doi: 10
521 .1016/j.icarus.2017.06.019
- 522 Steel, D., & Elford, W. (1991). The height distribution of radio meteors: com-
523 parison of observations at different frequencies on the basis of standard echo
524 theory. *Journal of Atmospheric and Terrestrial Physics*, 53(5), 409 - 417. doi:
525 10.1016/0021-9169(91)90035-6
- 526 Stober, G., Jacobi, C., & Singer, W. (2011). Meteoroid mass determination from un-
527 derdense trails. *Journal of Atmospheric and Solar-Terrestrial Physics*, 73(9),
528 895-900. (Scientific Results from Networked and Multi-instrument studies
529 based on MST Radar) doi: 10.1016/j.jastp.2010.06.009
- 530 Yee, K. S. (1966). Numerical solution of initial boundary value problems involving
531 maxwell's equations in isotropic media. *IEEE Trans. Antennas and Propaga-*
532 *tion*, 302–307.

Figure 1.

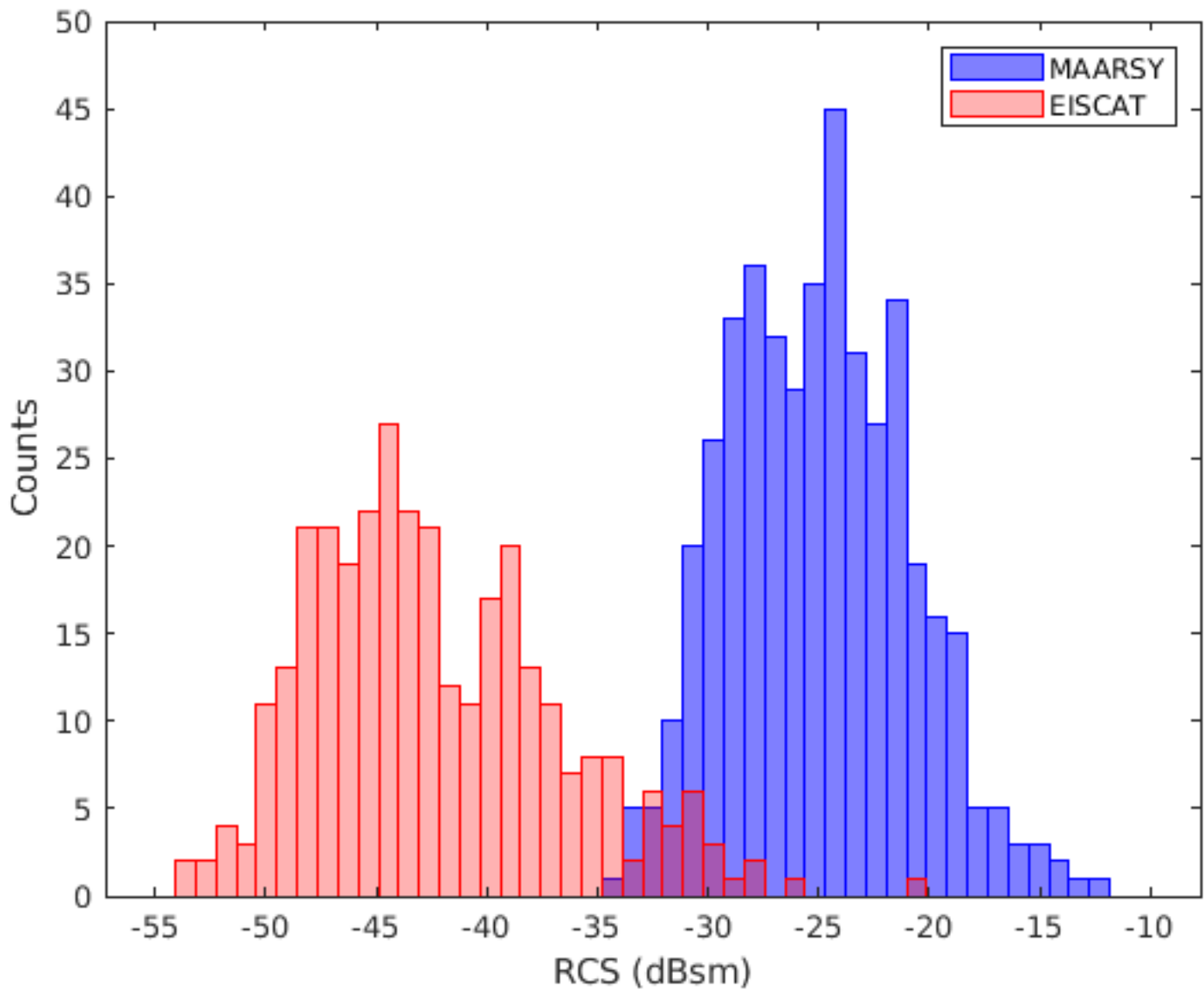


Figure 2.

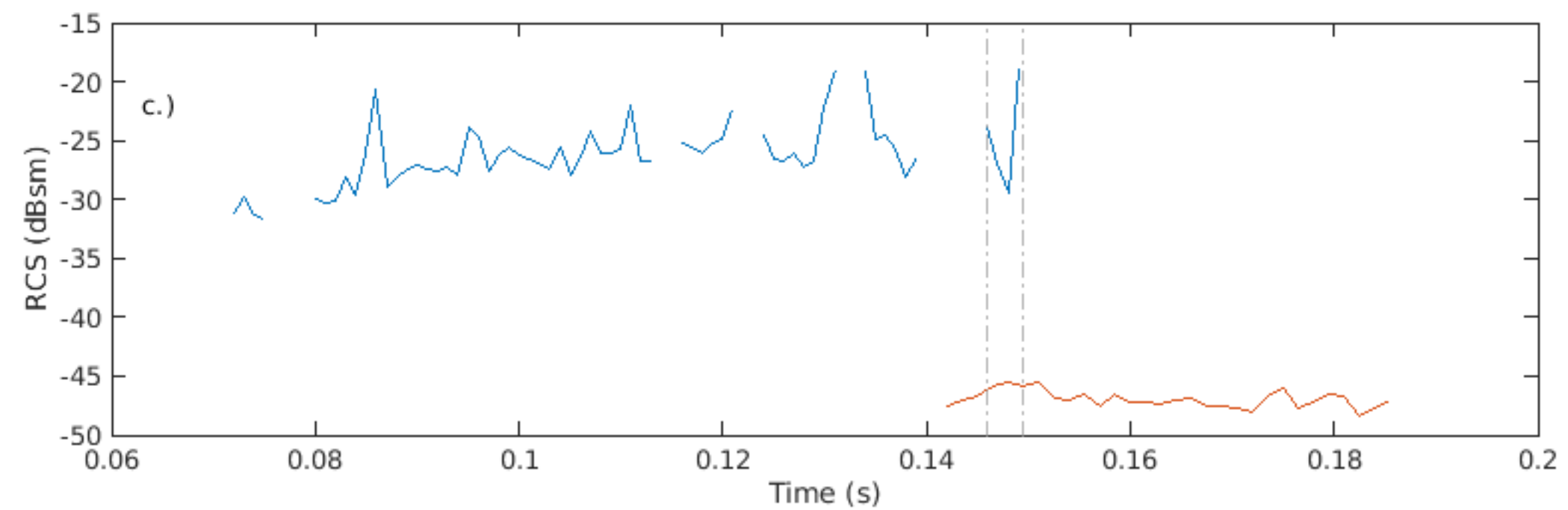
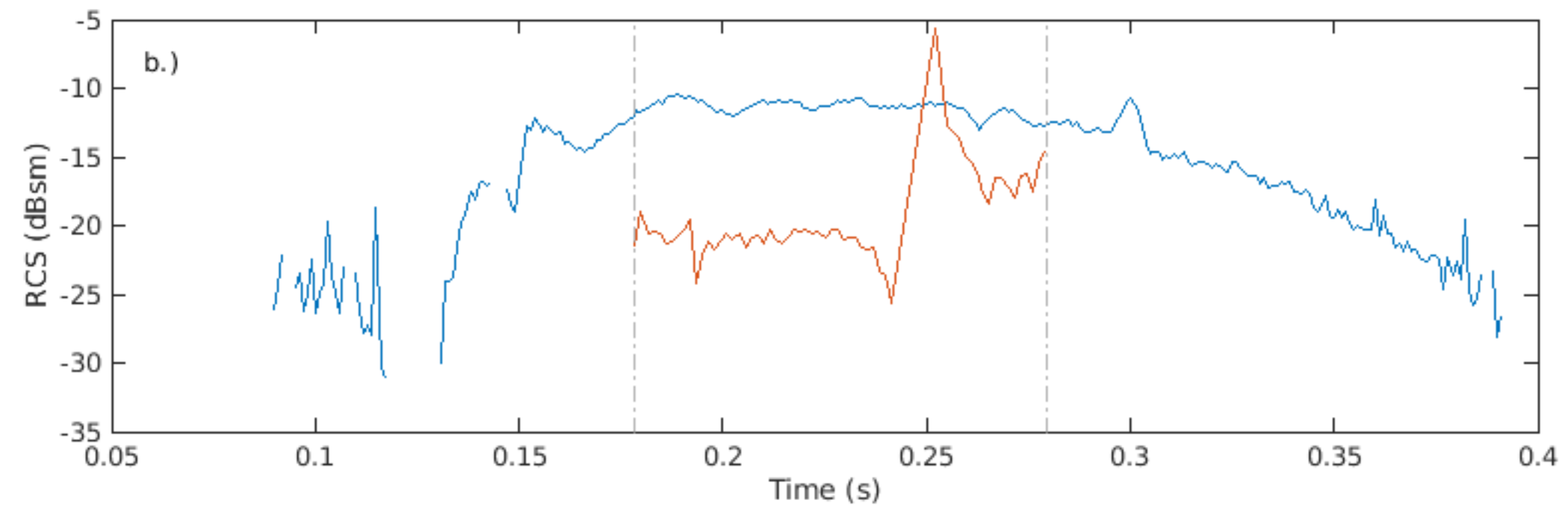
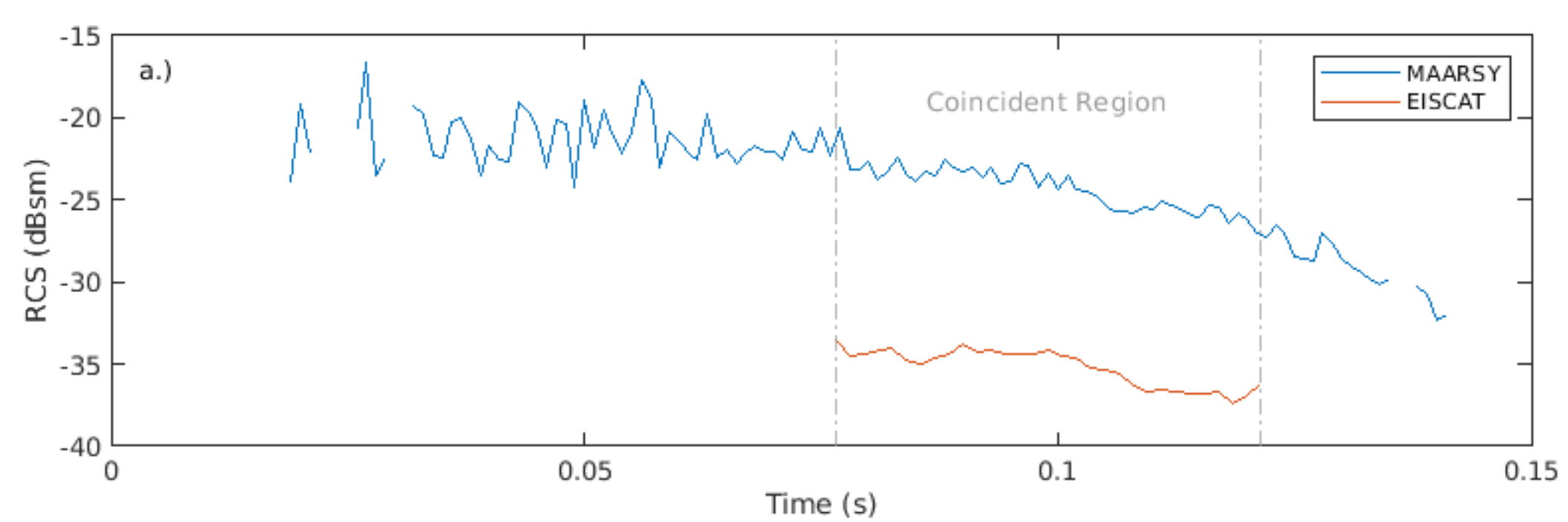


Figure 3.

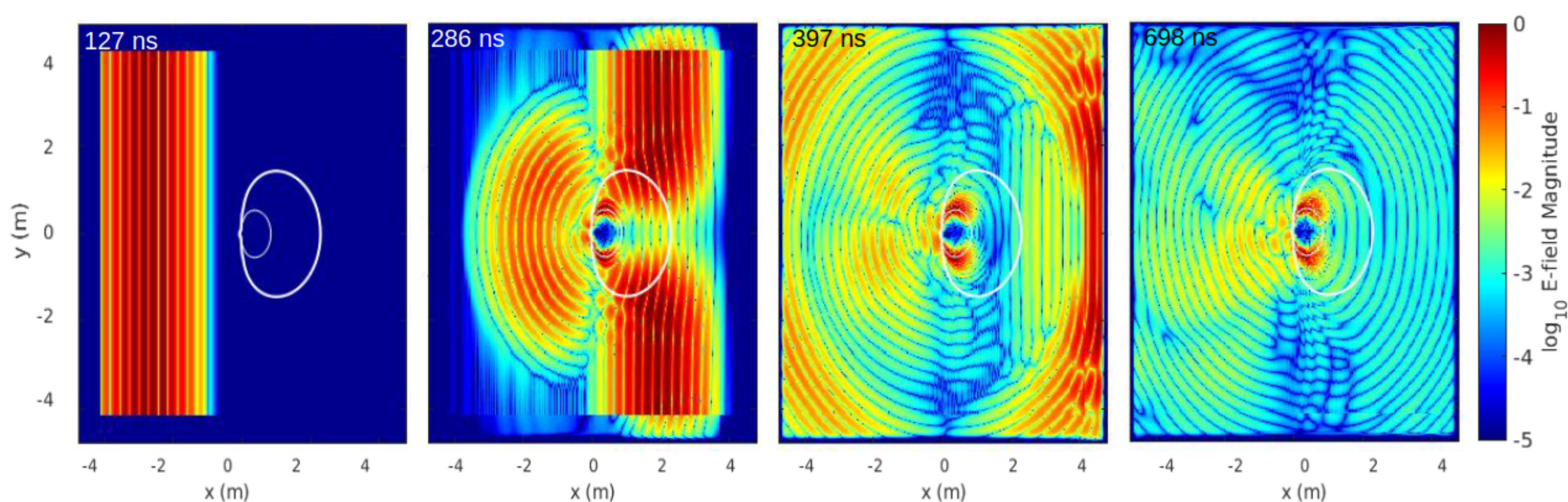


Figure 4.

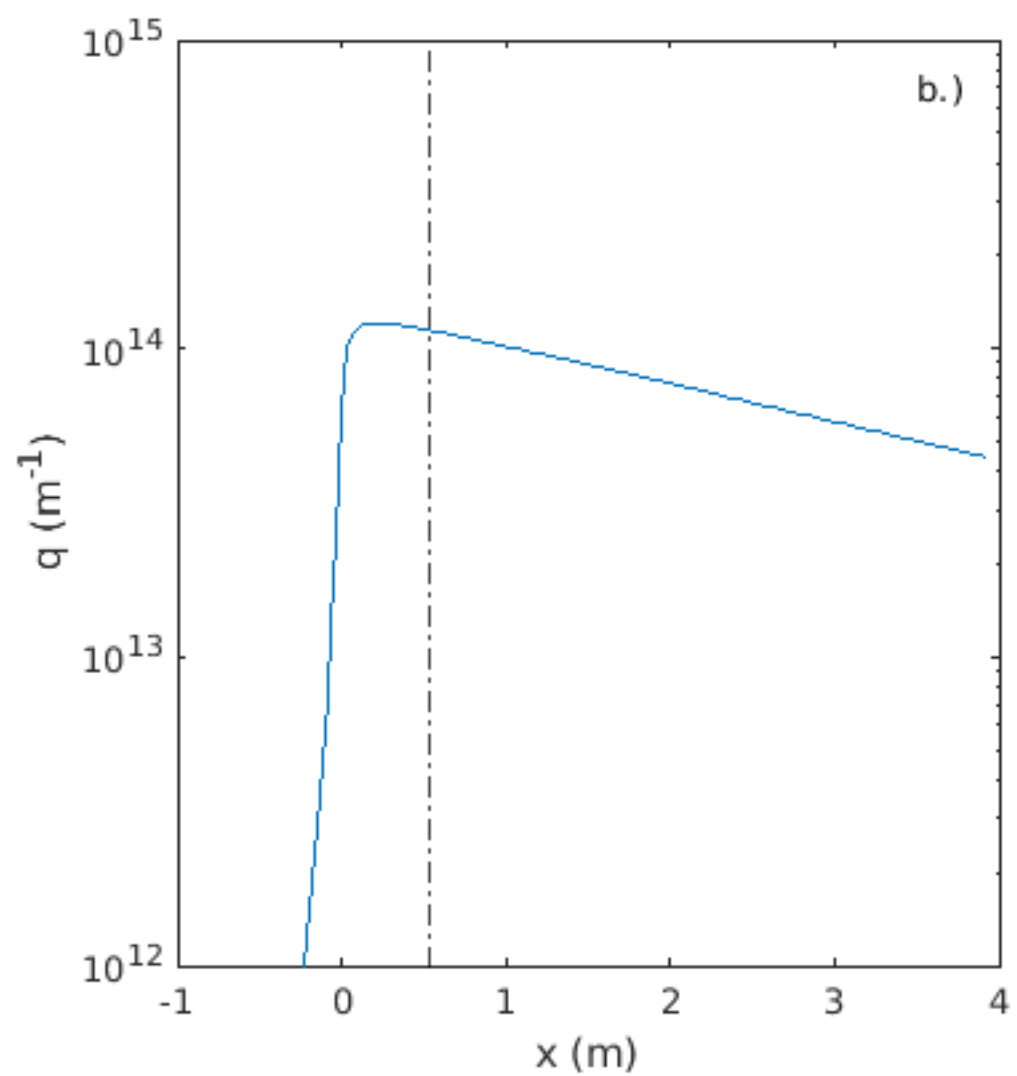
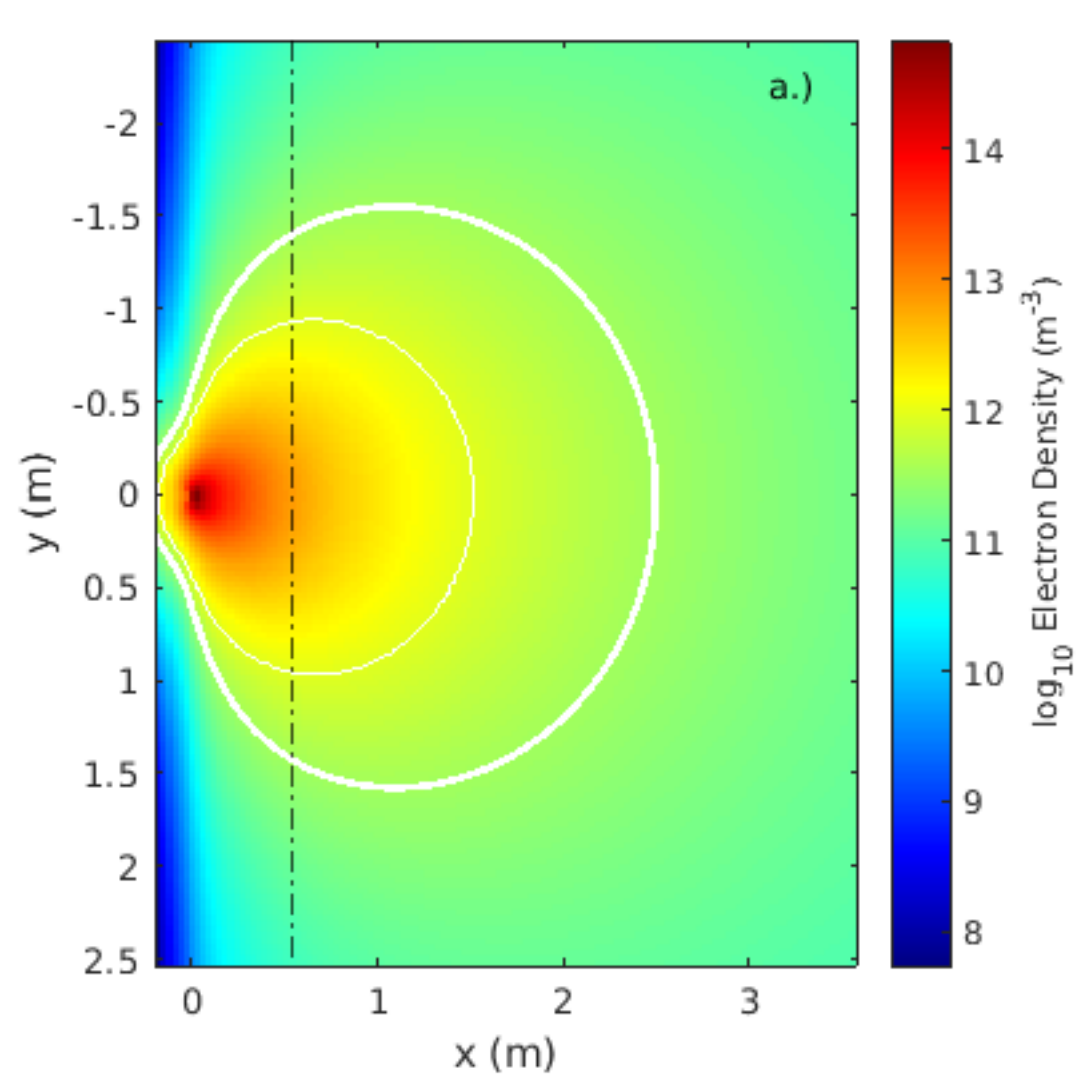
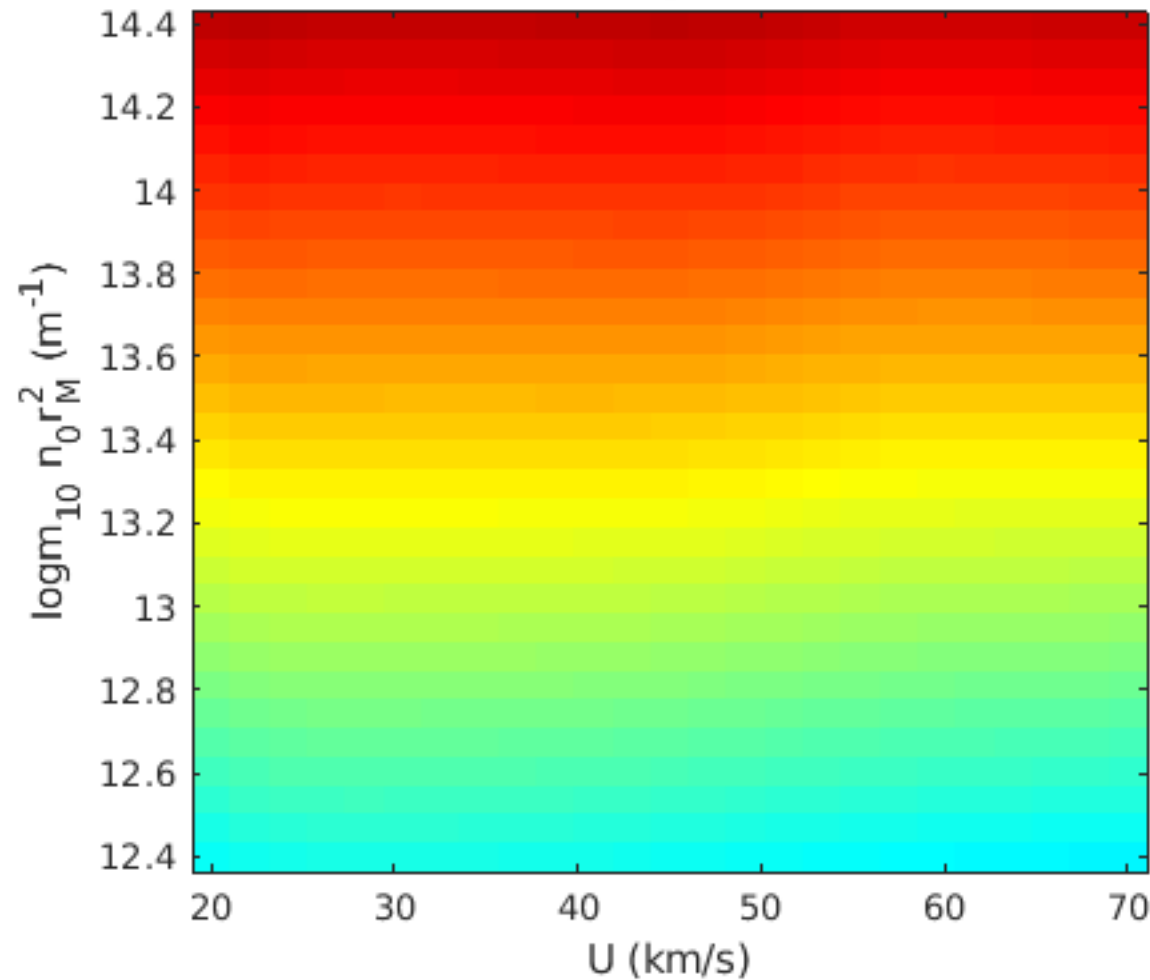
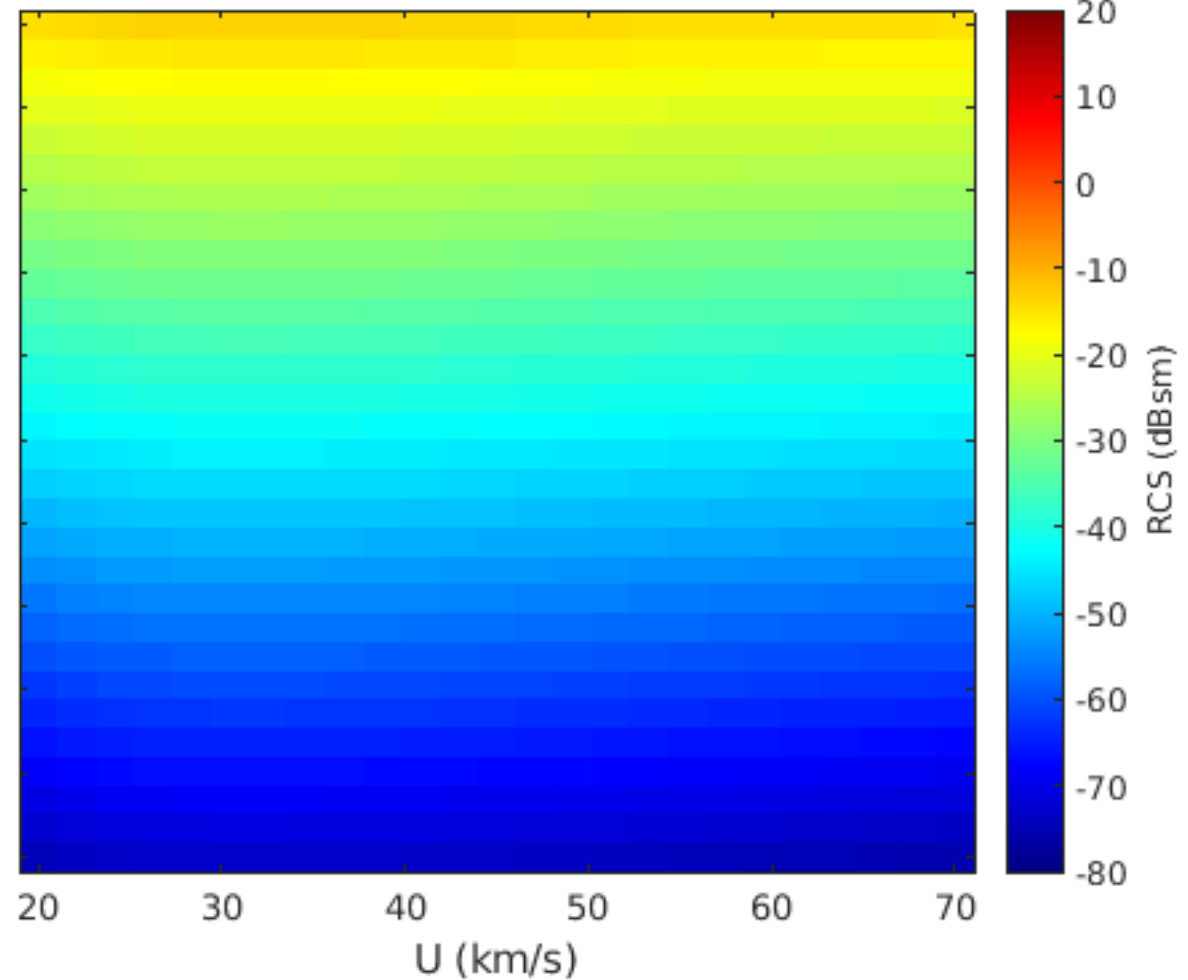


Figure 5.

MAARSY, 100 km



EISCAT, 100 km



RCS (dBsm)

20
10
0
-10
-20
-30
-40
-50
-60
-70
-80

Figure 6.

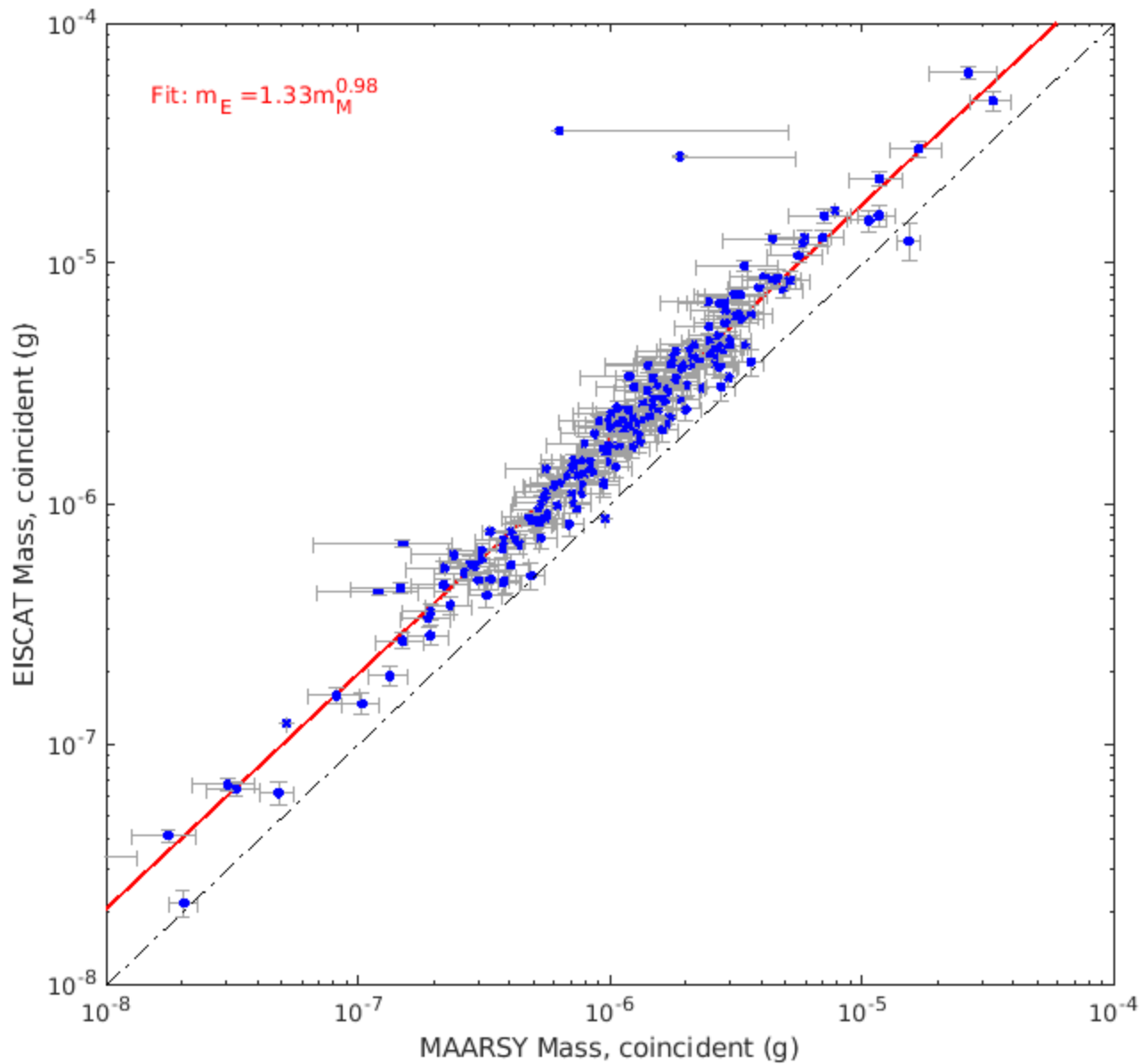


Figure 7.

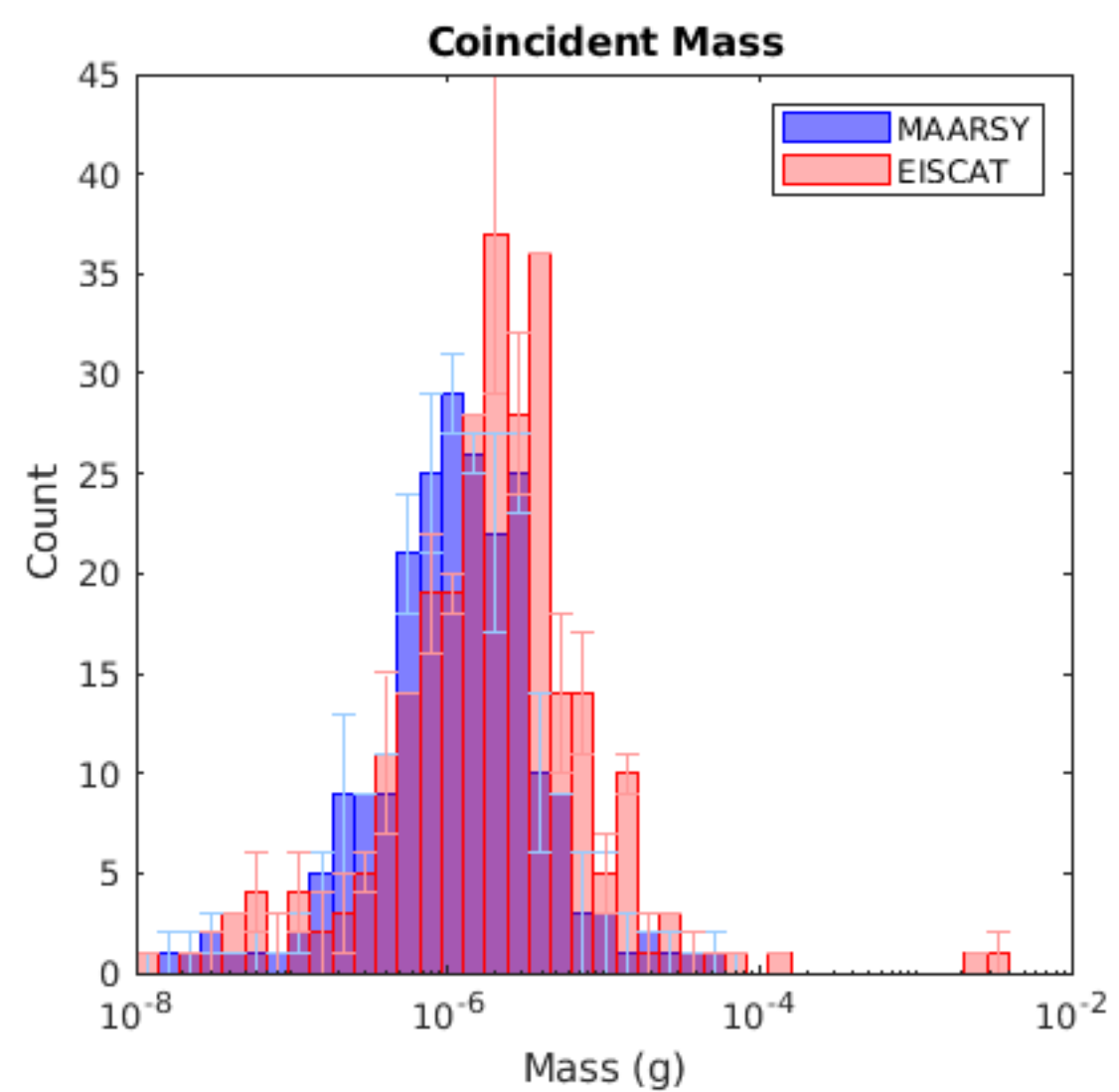
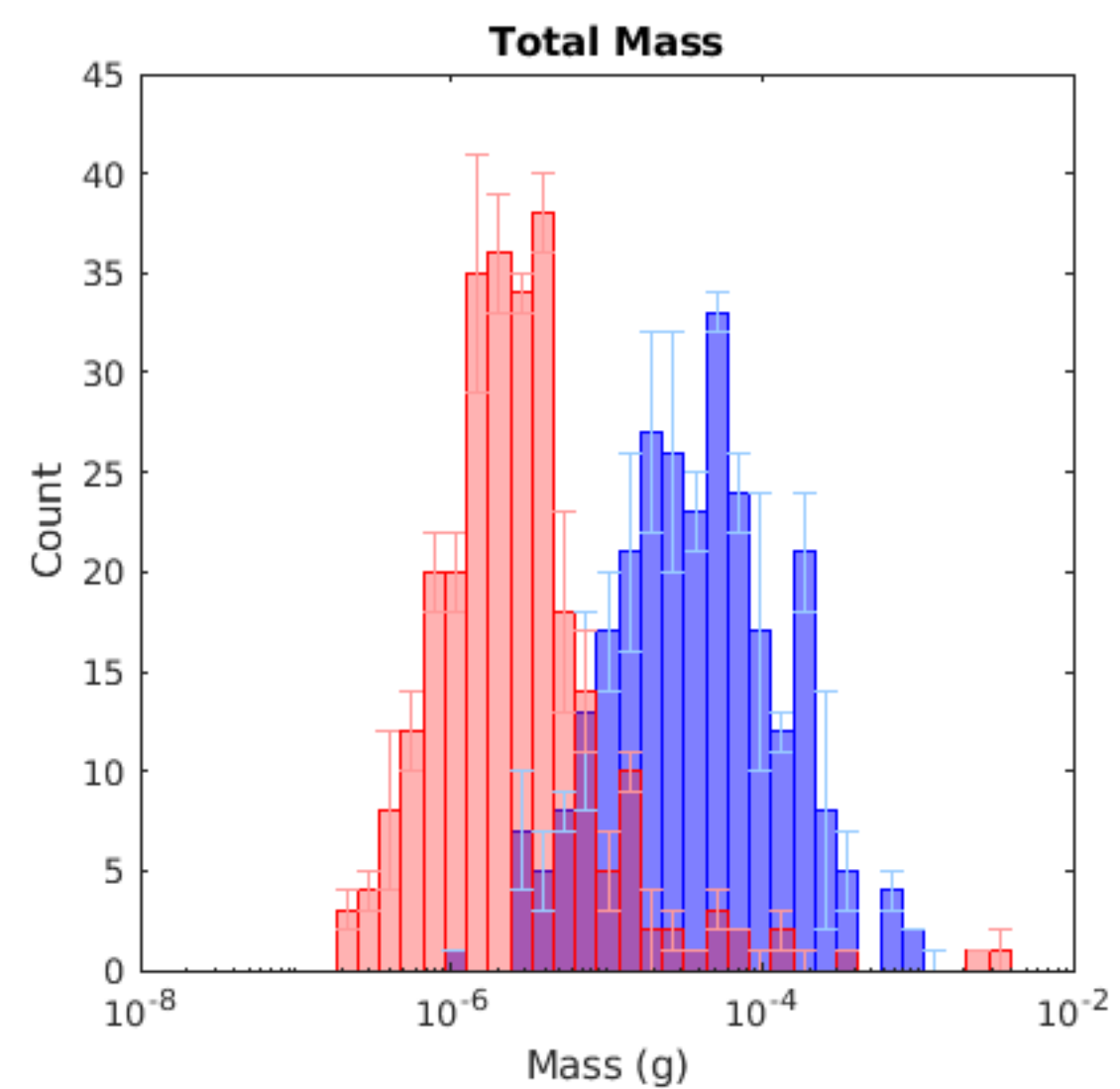


Figure 8.

